Solar Energy 305 (2026) 114276

Contents lists available at ScienceDirect

Solar Energy

journal homepage: www.elsevier.com/locate/solener

Chiral ligand-assisted interface modulation for reduced voltage loss in perovskite solar cells

Yu-Hung Hsiao [a], Lan-Sheng Yang [b], Shih-Han Huang [a], Hou-Chin Cha [a,c], Wen-Ting Li [a], Sheng-Long Jeng [d], Yu-Chiang Chao [b,*], Yu-Ching Huang [a,e,f,*]

[a] Department of Materials Engineering and Organic Electronics Research Center, Ming Chi University of Technology, New Taipei City 24301, Taiwan
[b] Department of Physics, National Taiwan Normal University, Taipei City 11677 Taiwan
[c] College of Engineering, Ming Chi University of Technology, New Taipei City 24301, Taiwan
[d] Department of Material Research, National Atomic Research Institute, Taoyuan City 325207, Taiwan
[e] Department of Chemical and Materials Engineering, Chang Gung University, Taoyuan City 33302, Taiwan
[f] Research Center for Critical Issues, Academia Sinica, Taipei City 115201, Taiwan

ARTICLE INFO

Keywords:
Perovskite solar cell
Chiral material
Open-circuit voltage
Non-radiative recombination

ABSTRACT

Perovskite solar cells (PSCs) have emerged as strong contenders for next-generation photovoltaic applications, owing to their exceptional optoelectronic characteristics and adjustable bandgaps. Despite these advantages, a notable discrepancy persists between the theoretical and experimentally achieved open-circuit voltage (Voc), largely attributed to interfacial energy misalignment and non-radiative recombination processes. In this work, we propose the introduction of chiral organic compounds into the perovskite precursor solution as a means to tailor the electronic structure and interfacial behavior of the absorber layer. Our systematic study reveals that the integration of chiral ligands not only promotes improved crystallinity of the perovskite films but also modulates lattice microstrain, as evidenced by X-ray diffraction (XRD) and microstrain analysis. Electrochemical impedance spectroscopy (EIS) results further indicate a reduction in charge transport resistance and interfacial recombination, confirming a more favorable electronic interface between the perovskite and charge transport layers. Importantly, the non-radiative voltage loss is significantly mitigated, decreasing from 354 mV in the control to 304 mV with chiral additive incorporation, thereby yielding an average Voc of 1.16 V. This study underscores the effectiveness of chiral molecular engineering in tuning film quality and interface properties. It also demonstrates a scalable strategy for enhancing PSC device efficiency, offering a promising pathway to close the Voc gap and advance perovskite-based photovoltaics toward greater performance and long-term operational stability.

1. Introduction

Organic-inorganic hybrid perovskite solar cells (PSCs) have garnered significant attention as next-generation photovoltaic devices due to their remarkable optoelectronic features. These include strong light absorption, low exciton binding energy, tunable optical bandgaps, and extended carrier diffusion lengths [1,2]. Within just a few decades of development, PSCs have demonstrated power conversion efficiencies (PCEs) exceeding 26 % [3], underscoring their rapid advancement. Furthermore, their suitability for large-scale production is supported by their low-cost raw materials [4,5], ease of solution-based fabrication, compatibility with flexible substrates [6–8], adaptability in tandem architectures [9,10], positioning them as a key technology in solar energy research. Among various device configurations, the inverted p-i-n architecture is often preferred due to its superior operational stability and reduced hysteresis compared to the conventional n-i-p setup [11,12]. However, inverted PSCs generally exhibit lower PCEs than their regular counterparts. This performance gap is mainly attributed to issues such as crystallographic imperfections in the perovskite layer and interfacial non-radiative recombination, which impairs efficient charge transport [13,14]. One critical limiting factor is non-radiative recombination via trap states, which significantly lowers the open-circuit voltage (V_{OC}) of the device [14–16]. These trap-induced losses affect carrier dynamics, hinder mobility, and disrupt quasi-Fermi level

* Corresponding authors at: Department of Physics, National Taiwan Normal University, Taipei City 11677, Taiwan (Y.-C. Chao); Department of Materials Engineering and Organic Electronics Research Center, Ming Chi University of Technology, New Taipei City 24301, Taiwan (Y.-C Huang).
E-mail addresses: ycchao@ntnu.edu.tw (Y.-C. Chao), huangyc@mail.mcut.edu.tw (Y.-C. Huang).

https://doi.org/10.1016/j.solener.2025.114276
Received 22 August 2025; Received in revised form 4 December 2025; Accepted 17 December 2025
Available online 22 December 2025

alignment between layers, leading to energy mismatches that further compromise V_{OC}. The V_{OC} in PSCs is governed by the energy difference between the quasi-Fermi levels of electrons and holes, which are influenced by the alignment of the Fermi levels at heterojunction interfaces. To mitigate V_{OC} losses, various strategies have been developed, including interface engineering [17,18], defect passivation [19], and the use of functional additive engineering [20,21]. For example, Liu et al. incorporated 1-butyl-3-methylimidazolium tetrafluoroborate ([BMIM]BF_4) between the SnO_2 electron transport layer (ETL) and the perovskite film. The Coulomb interaction between BF_4^- and Sn^{4+} modulated the surface work function of the ETL, resulting in better energy level alignment and improved charge extraction efficiency [22]. Similarly, S. Liu et al. explored the role of pentafluorobenzene derivatives bearing various functional groups such as hydroxyl, amino, and carboxyl in modifying the perovskite surface energetics. These groups coordinated with Pb atoms to form ordered dipolar layers, thereby adjusting the vacuum energy level. Their findings revealed that the unmodified perovskite surface exhibited a work function of 4.59 eV. Upon treatment with these polar molecules, the work function shifted to 4.27 eV (hydroxyl), 4.16 eV (amino), and 3.87 eV (carboxyl), respectively. Notably, the carboxyl-modified devices achieved a V_{OC} increase from 1.14 V to 1.19 V [23]. These studies highlight that the strategic incorporation of polar molecules to fine-tune energy level alignment between the perovskite and charge transport layers offers a promising pathway to minimize V_{OC} losses and enhance device efficiency.

Large organic cations, especially those with bulky aromatic or aliphatic groups, are inherently hydrophobic and can serve as moisture barriers by forming a protective coating over perovskite grains. This hydrophobic layer helps to enhance the environmental stability of PSCs by mitigating water ingress [24–26]. In one study, Zhao et al. employed various aromatic amine-based molecules, such as aniline, benzylamine, and phenylethylamine, to passivate the surface of 3D perovskite films [27]. Similarly, Lin et al. investigated the influence of 1-naphthylmethylamine (NMA) as an additive in $MAPbI_3$ perovskites. They observed that large cations tend to accumulate at grain boundaries during film formation, effectively passivating defect sites at those boundaries. This passivation suppressed non-radiative recombination at interfaces, resulting in a V_{OC} enhancement from 1.06 V to 1.16 V compared to the control [28]. However, such large-sized cations often contain long alkyl chains with insulating characteristics, which can impair charge transport and overall device performance.

In recent years, chiral materials have attracted growing attention due to their unique properties, including optical activity [29], second harmonic generation [30], and ferroelectric behavior [31]. Their structural compatibility with perovskite materials has led to widespread application in areas like optoelectronic sensing [32,33], light-emitting diodes [34], biomedical imaging [35], and photovoltaics [36–38]. Gao et al. introduced chiral molecules, S-/R-/*rac*-α-Methylbenzylamine (MBA), into $FASnI_3$ perovskite systems. This resulted in the formation of a two-dimensional chiral interfacial layer between PEDOT:PSS and the perovskite, which facilitated improved hole transport and better energy level alignment, attributed to the chiral-induced spin selectivity (CISS) effect [39]. In another example, Huang et al. applied chiral β-methylphenethyl ammonium iodide (MPAI) to passivate $FA_{1-X}MA_XPbI_3$ perovskite. By controlling the annealing process, they successfully constructed 1D@3D and 2D@3D heterostructures. The optimized 2D@3D devices exhibited a PCE of 22.19 %, and unencapsulated cells retained 98 % of their initial efficiency after 1300 h of ambient storage (30 % RH, 20 °C) [40]. While these results underscore the potential of chiral molecules in PSCs, their specific impact on V_{OC} reduction remains underexplored. Furthermore, prior approaches frequently employ bulky organic cations that readily induce quasi-2D or 2D phases, complicating the interpretation of interfacial energetics and limiting scalability [41,42]. A clear mechanistic framework linking molecular chirality, interfacial dipole formation, quasi-Fermi level splitting, and Voc modulation is notably absent from current literature, particularly for CsFA-based perovskite systems used in high-performance inverted devices. To address this critical knowledge gap, we propose a small-molecule chiral ligand strategy that avoids undesired low-dimensional phase formation while enabling precise interfacial dipole engineering.

In this study, we hypothesize that the inherent molecular asymmetry of chiral ligands induces dipole moments that can favorably influence energy level alignment in perovskites. To test this, we formulated a precursor solution by combining R-methylbenzylammonium iodide (R-MBAI) with lead iodide, creating the compound R-$MBPbI_3$. We then incorporated this chiral additive into CsFA-based mixed-halide PSCs at various concentrations. These results revealed a consistent improvement in open-circuit voltage, with V_{OC} increasing by approximately 0.03–0.04 V, from 1.13 V to 1.17 V. These findings demonstrate that introducing chiral additives offers a simple yet effective strategy to modulate surface energetics and reduce V_{OC} losses, thereby enhancing the overall photovoltaic performance of PSCs.

2. Methodology

2.1. Materials

The materials used in this study were all utilized without additional purification. Nickel acetate tetrahydrate ($Ni(CH_3COO)_2 \cdot 4H_2O$, 99.0 %) was obtained from Showa Chemical, Japan. A carboxylated derivative of poly(3-hexylthiophene-2,5-diyl) (P3HT–COOH, MW ≈ 90 kDa) was provided by Rieke Metals, USA. Ethanolamine (99 %) and ethyl acetate (99.8 %) were purchased from Acros Organics, USA. Formamidinium halide salts, specifically iodide (FAI, 99.99 %) and bromide (FABr, 99.99 %), were sourced from Greatcell Solar Materials, Australia. Cesium bromide (CsBr, 99.99 %) came from Thermo Fisher Scientific, USA. (6,6)-Phenyl-C_{61}-butyric acid methyl ester (PCBM, 99.8 %) was supplied by Luminescence Technology Corp. in Taiwan. Other key materials, such as cesium iodide (CsI, 99.99 %), lead bromide ($PbBr_2$, 99.999 %), and solvents including dimethyl sulfoxide (DMSO, 99.9 %), dimethylformamide (DMF, ≥99.9 %), chlorobenzene (CB, 99.9 %), isopropanol (IPA, 99.5 %), and ethanol (EtOH, 99.8 %) were purchased from Sigma-Aldrich, USA. Additionally, polyethyleneimine (PEI, branched form, average Mn ~ 10,000) was also acquired from the same supplier. Lead iodide (PbI_2, 99.999 %) was sourced from TCI, Japan.

2.2. Preparation of R-MBAI

To synthesize *R*-methylbenzylamine (*R*-MBAI), 10 mL of R-methylbenzylamine was first dissolved in 15 mL of ethanol and maintained in an ice-cooled environment. Under vigorous stirring, 13 mL of hydroiodic acid (HI) aqueous solution was slowly added dropwise to the chilled mixture. The reaction was allowed to proceed continuously for 10 h. After completion, the mixture was concentrated using a rotary evaporator equipped with a water bath at 95 °C, resulting in the formation of a solid residue. The obtained crude solid was rinsed thoroughly with cold diethyl ether to remove residual by-products and then subjected to vacuum drying. To further purify the product, recrystallization was performed using ethanol as the solvent, yielding transparent, colorless

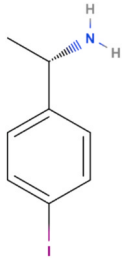

Fig. 1. The schematic diagram of *R*-MBAI.

crystals. The chemical structure of the final compound is illustrated in Fig. 1.

2.3. Preparation of precursor Solutions

To prepare the sol–gel-based NiO_X solution, 0.124 g of nickel acetate tetrahydrate was first dissolved in 1 mL of ethanol and stirred at 60 °C until a homogeneous and transparent solution formed. Following this, 30 μL of ethanolamine was introduced into the mixture. The resulting solution was then passed through a 0.22 μm poly(1,1,2,2-tetrafluoroethylene) (PTFE) membrane filter to eliminate particulates. For the P3HT-COOH solution, 0.5 mg of the polymer was completely dissolved in 1 mL of dimethylformamide (DMF) to ensure uniformity. The perovskite precursor solution was prepared at a concentration of 1.4 M using a solvent blend of DMF and dimethyl sulfoxide (DMSO) in a 4:1 vol ratio. To achieve a target optical bandgap of 1.74 eV, the precursor mixture included CsBr, FAI, FABr, and PbI_2, combined in a molar proportion of 0.4:0.1:0.5:1, respectively. The chiral component *R*-$MBAPbI_3$ was synthesized separately at a concentration of 0.7 M by dissolving equimolar amounts of *R*-MBAI and PbI_2 in the same DMF: DMSO (4:1) solvent system. For the electron transport layer (ETL), [6,6]-Phenyl-C_{61}-butyric acid methyl ester (PCBM) was used and prepared at 20 mg/mL in chlorobenzene (CB). Lastly, the work function modification layer (WFL) was formulated using polyethyleneimine (PEI) dissolved in isopropanol (IPA) at a concentration of 0.1 wt%.

2.4. Device fabrication

The p-i-n type device was constructed using the layer sequence: ITO/NiO_X/P3HT-COOH/Perovskite/PCBM/PEI/Ag. Indium tin oxide (ITO)-coated glass substrates were first cleaned through ultrasonic treatment by immersing them for 15 min each in a detergent solution followed by isopropanol. After drying with a nitrogen stream, the substrates underwent ultraviolet–ozone (UV-O_3) exposure for 30 min to improve surface wettability and remove organic residues. Deposition of the hole transport layers (HTLs), NiO_X and P3HT–COOH, was carried out in ambient air. The NiO_X sol–gel solution (60 μL) was applied to the substrate via spin-coating at 4000 rpm for 20 s, then subjected to thermal annealing at 300 °C for 6 min. Afterward, the P3HT–COOH layer was formed by spin-coating 50 μL of its solution under the same speed and duration, followed by heating at 140 °C for 10 min.

The perovskite photoactive layer was deposited inside a nitrogen-filled glovebox using a two-step spin-coating protocol with anti-solvent treatment. The precursor was first spun at 1000 rpm for 5 s, then at 5000 rpm for 30 s. At the 10-second mark of the second spin stage, 500 μL of ethyl acetate was swiftly dropped onto the rotating substrate to promote rapid crystallization. Subsequently, PCBM and PEI layers were deposited sequentially by spin-coating 50 μL of each solution at 1000 rpm and 3000 rpm, respectively, both for 30 s, under inert conditions. To complete the device, a 100 nm-thick silver (Ag) electrode was thermally evaporated on top. The device's effective area, defined by the Ag contact, measured 0.04 cm2.

2.5. Materials and devices characterization

The photovoltaic device performance was evaluated using a Keithley 2410 source meter (Keithley Instruments, Solon, OH, USA) under standard AM 1.5G solar simulation, with an irradiance intensity calibrated to 100 mW cm^{-2}. Structural characterization was performed through X-ray diffraction (XRD) analysis utilizing a Bruker D8 Discover A25 diffractometer (Bruker AXS GmbH, Karlsruhe, Germany), operating with Cu Kα radiation (λ = 1.5406 Å). Optical absorbance properties were determined via ultraviolet–visible (UV–Vis) spectroscopy using a V-750 spectrophotometer (JASCO, Tokyo, Japan). The external electroluminescence quantum efficiency (EL-EQE) was measured using an ELCT-3010 system (Enlitech) by applying an external voltage bias. Electrochemical impedance spectroscopy (EIS) was carried out on the Paios characterization platform (Fluxim AG), a multifunctional system designed for the electrical assessment of photovoltaic devices. External quantum efficiency (EQE) spectra were obtained using a quantum efficiency measurement system (QE-R, Enlitech), based on photon-to-electron conversion analysis. Chiroptical characterizations included circular dichroism (CD), which was recorded using a JASCO J-1500 spectropolarimeter, and circularly polarized luminescence (CPL), collected with a JASCO CPL-300 instrument. In addition, magnetic field-dependent optical measurements were conducted using JASCO PM-491 permanent magnets at various field strengths, with data acquired at a scattering angle fixed at 0°.

3. Results and discussion

Although chiral molecules exist as two enantiomeric forms (R and S), our preliminary screening experiments revealed that *R*-MBAI produced more stable film formation and more reproducible device improvements compared with its S-configured counterpart. Devices incorporating *S*-MBAI showed comparable or slightly inferior performance relative to *R*-MBAI and did not exhibit clear concentration-dependent trends, making it difficult to draw meaningful or statistically supported conclusions. Relevant data for *S*-MBAI, which was not pursued in depth, are provided in Supplementary Information (Fig. S1). Given the lack of clear, reproducible trends for *S*-MBAI, this study focuses on *R*-MBAI as the more effective chiral ligand, while acknowledging that a systematic comparison of R/S enantiomers will be an important direction for future work to further elucidate chirality-dependent interfacial modulation. To investigate the effect of chiral additives, we incorporated varying concentrations of *R*-$MBAPbI_3$ (1 mol%, 3 mol%, and 5 mol%) into the perovskite precursor solution and systematically compared the photovoltaic performance of devices with and without the additive. The devices followed a p-i-n configuration of ITO/NiO_X/P3HT-COOH/perovskite/PCBM/PEI/Ag. Device performance metrics are summarized in Fig. 2, and detailed photovoltaic parameters are listed in Table 1. The reference device, fabricated without *R*-$MBAPbI_3$, showed an initial V_{OC} of 1.14 V. Upon the addition of 1 mol% *R*-$MBAPbI_3$, V_{OC} increased to 1.17 V, while Jsc and FF remained largely unchanged. When the concentration of the chiral additive was raised to 3 mol% and 5 mol%, the average Jsc exhibited a slight decline to 17.79 mA/cm^2 and 17.89 mA/cm^2, respectively. However, the FF showed a marked decrease, dropping to 55.21 % and 46.84 %, respectively. During the initial optimization process, a broader concentration range of the chiral ligand was examined (Fig. S2). Extremely low concentrations resulted in negligible changes in the perovskite layer, whereas overly high concentrations led to unstable crystallization and pronounced formation of low-dimensional perovskite phases, causing significant statistical variability. Therefore, the four representative concentrations (0, 1, 3, and 5 mol%) were selected for detailed investigation, as they consistently produced meaningful and reproducible trends. According to the J–V curves presented in Fig. S3, the reduction in FF at higher additive concentrations can be attributed to increased parallel resistance, likely caused by the excessive incorporation of *R*-$MBAPbI_3$. Interestingly, the device group with 1 mol% additive demonstrated a noticeably narrower PCE distribution compared to the additive-free devices, suggesting improved film uniformity and better process reproducibility when the chiral additive is used at optimized levels.

To elucidate the influence of chiral additives on the structural properties of perovskite films, XRD measurements were conducted across a range of additive concentrations. Particular attention was given to the primary (110) diffraction peak of the perovskite phase, which exhibited a progressive shift as the chiral additive concentration increased. As illustrated in Fig. 3a, the (110) peak positions for additive concentrations of 0, 1, 3, and 5 mol% appeared at 14.32°, 14.29°, 14.28°, and 14.26°, respectively. This gradual shift toward lower angles indicates a lattice expansion. Concurrently, an increase in the intensity

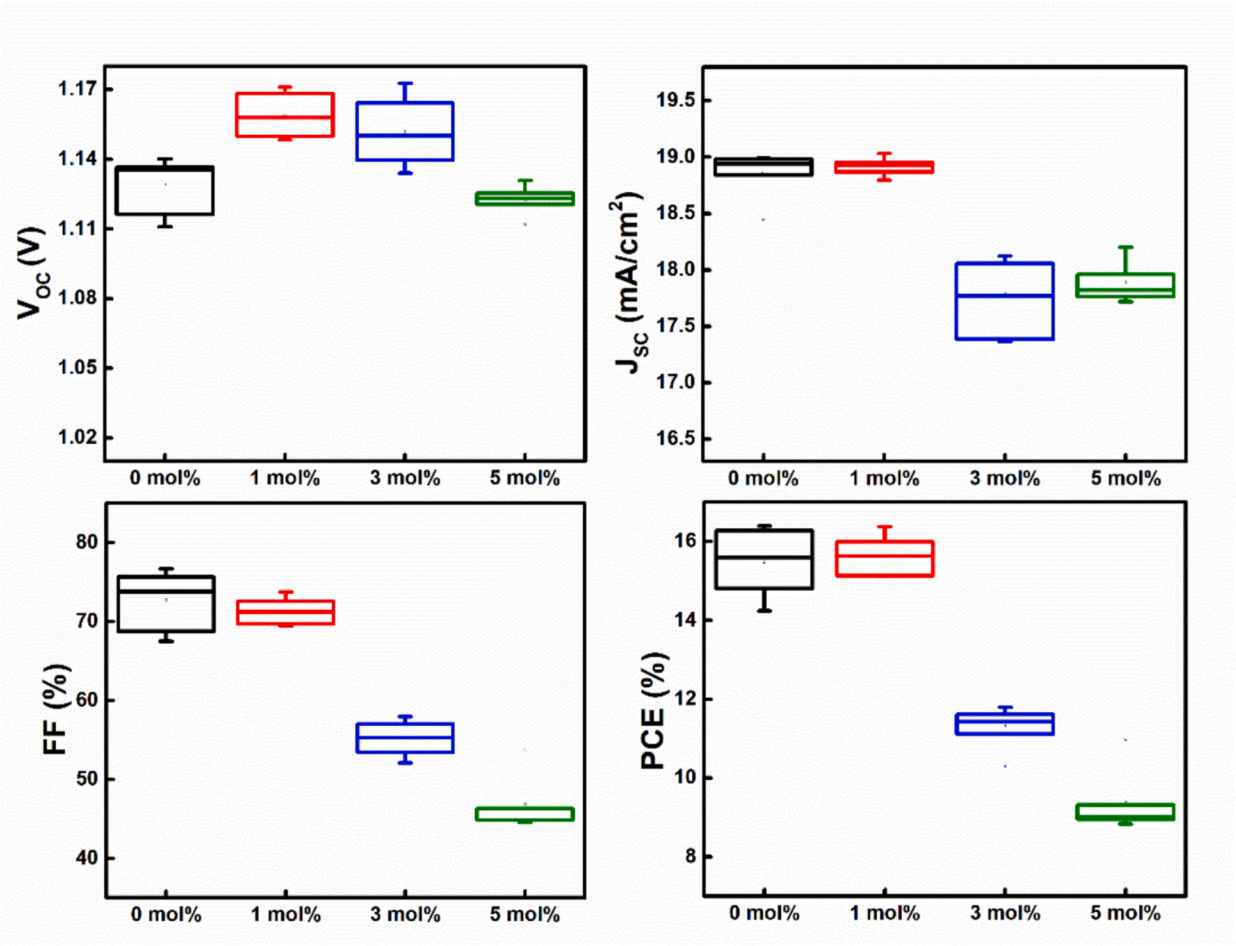

Fig. 2. Distribution of V_{OC}, J_{SC}, FF, and PCE of the PSCs fabricated from the perovskite precursor with different R-MBAPbI$_3$ concentrations.

Table 1
Photovoltaic characteristics of the PSCs fabricated from the perovskite precursor with different *R*-MBAPbI$_3$ concentrations. These values correspond to the champion PCEs, while the averages from 10 devices are provided in parentheses.

Concentration (mol%)	V_{OC} (V)	J_{SC} (mA/cm^2)	FF (%)	PCE (%)
0	1.14 (1.13 ± 0.01)	18.84 (18.86 ± 0.21)	76.65 (72.70 ± 3.74)	16.40 (15.48 ± 0.84)
1	1.17 (1.16 ± 0.01)	18.96 (18.92 ± 0.07)	73.74 (71.26 ± 1.64)	16.37 (15.62 ± 0.48)
3	1.15 (1.15 ± 0.01)	18.12 (17.79 ± 0.31)	56.54 (55.21 ± 2.11)	11.79 (11.31 ± 0.49)
5	1.12 (1.12 ± 0.01)	18.20 (17.89 ± 0.19)	53.66 (46.84 ± 3.87)	10.97 (9.41 ± 0.89)

of the PbI_2-related peaks was observed with higher additive content. This angular shift is attributed to the incorporation of the relatively bulky chiral cation into the A-site of the perovskite lattice, which slightly distorts the crystal structure. Using Bragg's law, the corresponding interplanar spacings were determined to be 6.38 Å (0 mol%), 6.39 Å (1 mol%), 6.40 Å (3 mol%), and 6.41 Å (5 mol%), confirming a subtle expansion of the lattice with increasing additive content. Furthermore, at higher concentrations of the chiral additive, diffraction patterns suggest the emergence of quasi-two-dimensional (2D) perovskite phases, as depicted in Figs. 3b and 3c. This structural transformation implies that excessive additive loading leads to disordered quasi-2D configurations, which hinder efficient charge transport and ultimately contributing to reduced J_{SC} and FF values [41]. As the quasi-2D domains become more pronounced with increasing *R*-MBAPbI$_3$ content, their quantum-well-like layered arrangement introduces additional barriers for vertical carrier transport and increases interfacial resistance [43]. In contrast, when a small amount of *R*-MBAPbI$_3$ is introduced (1 mol%), the structural perturbation remains minimal, and the chiral ligand primarily acts at the interface, where it passivates shallow trap states and induces a favorable interfacial dipole. Such interfacial modification suppresses non-radiative recombination and can account for the increase in V_{OC} observed at low *R*-MBAPbI$_3$ loading, consistent with the photovoltaic characteristics of the devices described earlier. To assess whether the chiral additives introduce lattice distortion or internal stress, we analyzed the broadening of the XRD peaks through full width at half maximum (FWHM) values and constructed Williamson-Hall (W-H) plots for each condition. The slope of these plots allowed estimation of the microstrain present in the perovskite films, as shown in Figs. 3d–3h. According to Fig. 3h, the microstrain in the film without any additive was calculated as 7.01×10^{-4}. Upon incorporating 1 mol% *R*-MBAPbI$_3$, the microstrain increased substantially to 1.16×10^{-3}, indicating notable lattice distortion. Interestingly, when the additive concentration was further raised to 3 mol% and 5 mol%, the strain levels began to decline, suggesting possible relaxation or structural reorganization. In addition, a slight deviation is observed in the W-H plots near the 1.2 region of 4sinθ (Figs. 3d-3g). This feature arises from partial overlap between the perovskite (310) diffraction peak and a weak PbI_2-related shoulder at higher diffraction angles, which broadens the peak profile and produces an upward bending in the W-H plot. Such behavior

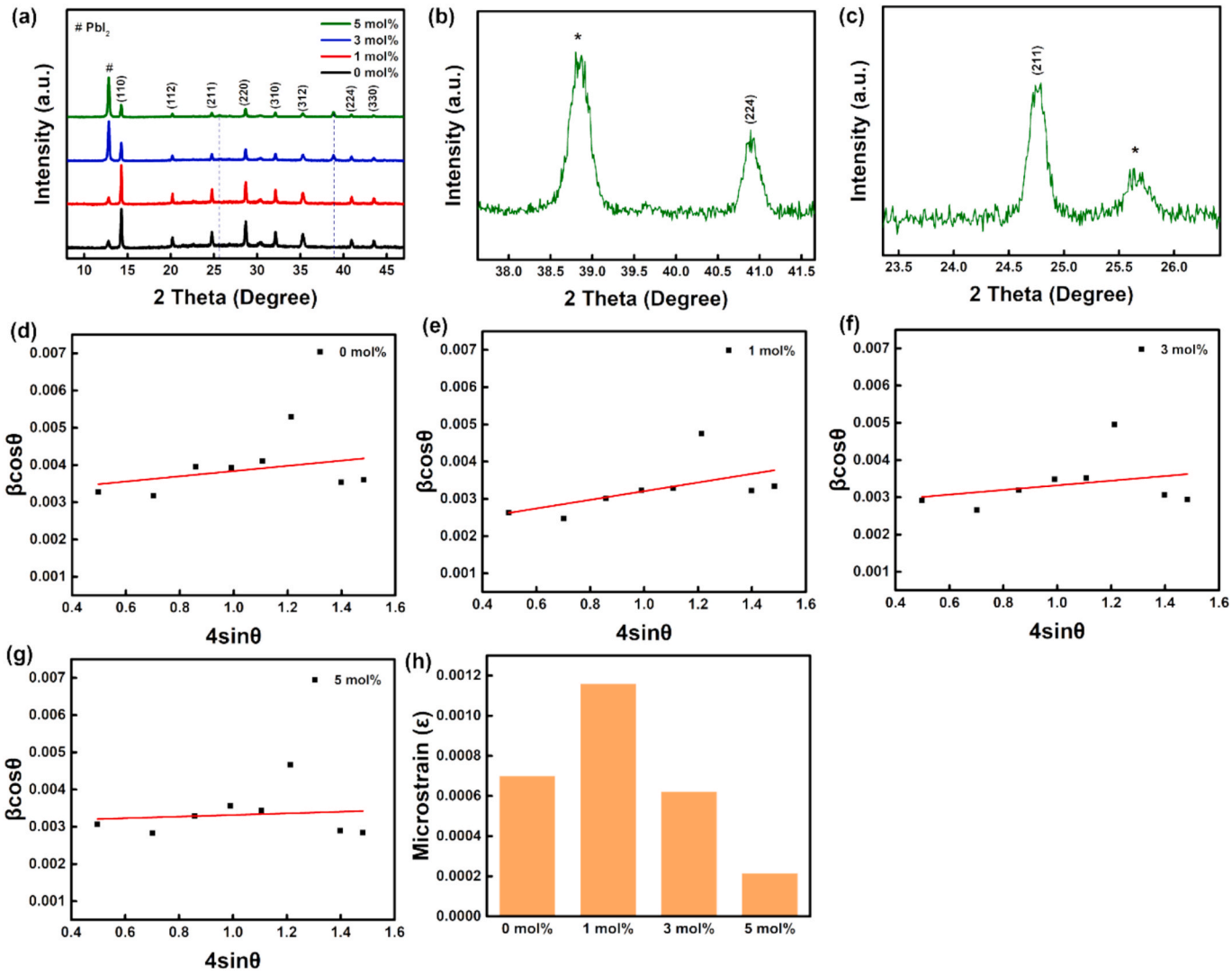

Fig. 3. (a) XRD pattern of different concentrations on perovskite film. XRD patterns of perovskite with 5 mol% *R*-MBAPbI$_3$ at (b) 25.63and (c) 38.83. (d)-(g) Williamson-Hall plot and (g) microstrain at different *R*-MBAPbI$_3$ concentrations in perovskite.

has been reported in strained or compositionally nonuniform perovskite systems [44]. Importantly, this angular region is excluded from the linear fitting used to extract the lattice microstrain and crystallite size, ensuring that the derived structural parameters remain accurate and representative of the intrinsic perovskite lattice. To deepen the analysis, we focus the subsequent discussion on two key samples: one without the chiral additive (w/o *R*-MBAPbI$_3$) and another with 1 mol% loading (w/ *R*-MBAPbI$_3$), where the structural and performance differences are most pronounced.

To explore the influence of the chiral additive R-MBAPbI$_3$ on the chiroptical behavior of perovskite films, measurements were performed on samples with and without the additive under varying magnetic field conditions. The digital pictures of the testing parameters for circular dichroism (CD) and circularly polarized luminescence (CPL) measurements are added in Fig. S4. The results, including CD, absorption (A) and g_{abs} spectra are presented in Fig. 4a–c and Supplementary Fig. S5. The dissymmetry factor for absorption g_{abs} was computed using the equation: $g_{abs} = \frac{\Delta A}{A} = \frac{CD(mdeg)}{32980 \times A}$. As illustrated in Fig. 4a, negligible CD signals were detected when no magnetic field was applied (0 T), which is likely due to the low loading (1 mol%) of the chiral component in the film. However, upon application of external magnetic fields at + 1.6 T and –1.6 T, derivative-like CD features emerged near the band-edge absorption, as shown in Fig. S5. This spectral change is attributed to Zeeman splitting, where the external magnetic field lifts the degeneracy of the electronic states, resulting in multiple discrete energy levels that depend on the field strength and direction. In addition, the CPL, PL and g_{lum} were analyzed and are shown in Fig. 4d–f and Fig. S6. The g_{lum} values were calculated using the following expression: $g_{lum} = 0.000069913 \times ellipticity(mdeg)/DC(V)$, where the DC voltage represents the intensity of the non-polarized PL signal. Similar to the CD results, the CPL spectra under zero magnetic field exhibited no distinct chiroptical activity. However, under + 1.6 T and –1.6 T fields, mirror-symmetric CPL features were observed in the wavelength range of 650–850 nm, indicating magnetic-field-induced chiral emission behavior. Taken together, these observations suggest that in the absence of a magnetic field, both CD and CPL responses are minimal, likely due to the low concentration of *R*-MBAPbI$_3$. Therefore, the improvements in device performance associated with the additive are unlikely to stem from its intrinsic chiroptical effects under standard operating conditions.

It has been previously reported that the electronic band structure of perovskite materials is mainly determined by the orbital interactions of their constituent atoms. Specifically, the conduction band minimum (CBM) is predominantly governed by the hybridization of B-p orbitals and X-s orbitals, while the valence band maximum (VBM) is largely influenced by B-s orbitals and X-p orbitals. When strain is introduced

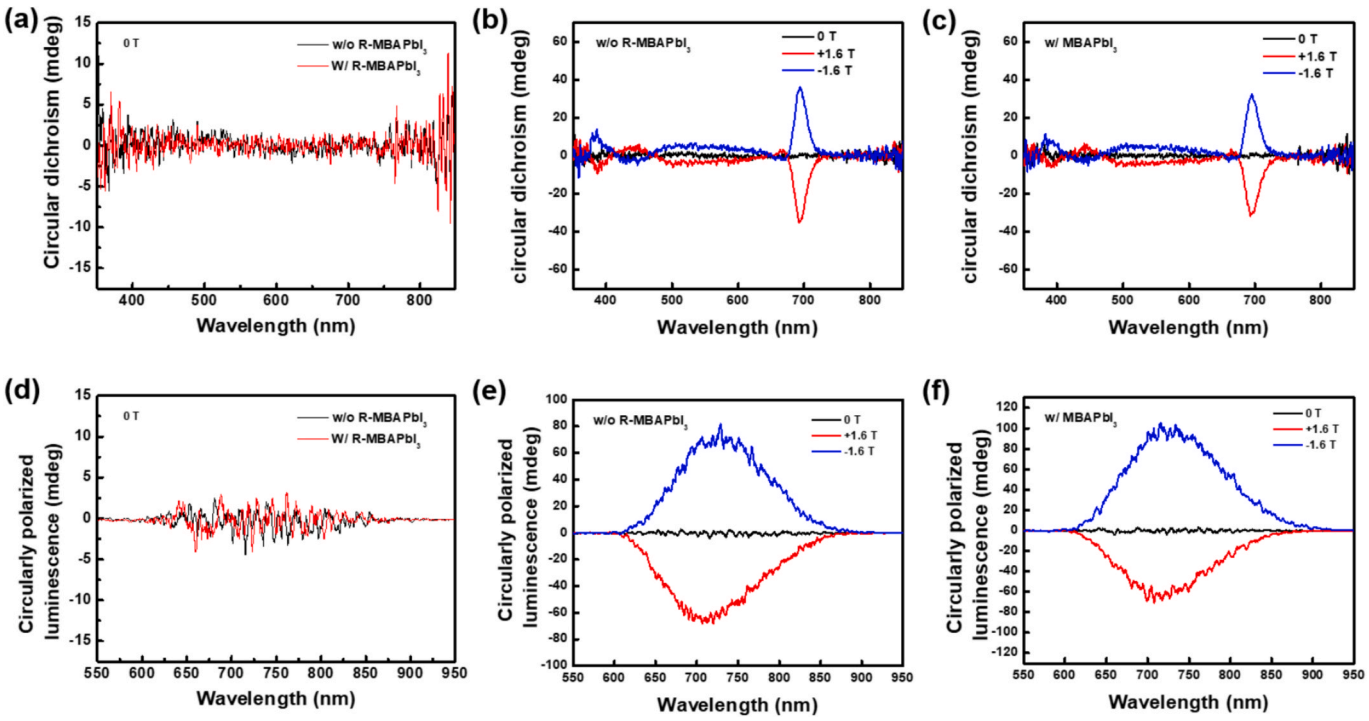

Fig. 4. (a)-(c) CD spectra and (d)-(f) CPL spectra of samples with and without *R*-MBAPbI$_3$ additive under various magnetic fields.

into the perovskite lattice, it results in distortion of the crystal framework, leading to changes in interatomic distances and, consequently, shifts in the energy levels [42,45]. As illustrated in Fig. 5a, incorporation of the chiral additive *R*-MBAPbI$_3$ into the perovskite film results in a notable reduction in the work function. This suggests that lattice strain induced by the bulky chiral cation modifies the material's electronic structure by altering its band alignment. To further explore the implications of this structural modulation on interfacial charge transport, electrochemical impedance spectroscopy (EIS) measurements were conducted under dark conditions with an external bias, spanning a frequency range from 1 MHz to 10 Hz (Fig. 5b). The impedance results indicate that devices incorporating R-MBAPbI$_3$ possess a higher recombination resistance (R_{rec}) relative to control devices without the additive, implying more suppressed carrier recombination. In parallel, EQE measurements (Fig. 5c) revealed enhanced photoresponse in the *R*-MBAPbI$_3$-based devices, which we attribute to improved energy level alignment at the interface between the perovskite and adjacent charge transport layers. This optimized alignment effectively minimizes interfacial energy barriers, thereby facilitating more efficient charge extraction and transport, which ultimately contributing to the observed performance enhancement in the device.

To conclude our investigation, we quantified the V_{OC} losses in the fabricated devices, as depicted in Fig. 5d, with corresponding numerical values summarized in Table 2. Based on the Shockley–Queisser (S-Q) theoretical framework, the total V_{OC} loss in photovoltaic devices can be categorized into three distinct components, as outlined below [46,47]:

$$q\Delta V = E_g - qV_{OC}$$

$$= \left(E_g - qV_{OC}^{SQ}\right) + \left(qV_{OC}^{SQ} - qV_{OC}^{rad}\right) + \left(qV_{OC}^{rad} - qV_{OC}\right)$$

$$= \left(E_g - qV_{OC}^{SQ} + \Delta qV_{OC}^{SC}\right) + \Delta qV_{OC}^{rad} + \Delta qV_{OC}^{non-rad}$$

$$= q(\Delta V_1 + \Delta V_2 + \Delta V_3)$$

In this analysis, q denotes the elementary charge, ΔV represents the total V_{OC} loss, E_g refers to the perovskite's optical bandgap, V_{OC}^{SQ} corresponds to the theoretical maximum V_{OC} as defined by the Shockley–Queisser limit, qV_{OC}^{rad} accounts for V_{OC} under purely radiative recombination, and $V_{OC}^{non-rad}$ includes contributions from both radiative and non-radiative recombination. Among the total voltage loss, ΔV_1 signifies the fundamental thermodynamic limitation, which is fixed at 284 mV for both reference and *R*-MBAPbI$_3$-modified devices due to intrinsic material properties. The second component, ΔV_2, is associated with charge carrier recombination losses during transport. Calculations revealed that ΔV_2 was 139 mV for the control device, while it decreased to 122 mV in the *R*-MBAPbI$_3$-incorporated device, indicating improved carrier extraction. The third component, ΔV_3, arises from non-radiative recombination processes. Devices without the chiral additive exhibited a ΔV_3 of 354 mV, which was significantly reduced to 304 mV upon incorporation of *R*-MBAPbI$_3$. These findings strongly suggest that the inclusion of the chiral additive facilitates better energy level alignment and enhances charge transport efficiency, while simultaneously suppressing non-radiative losses, thereby contributing to the overall improvement in device performance.

4. Conclusion

This work presents a comprehensive investigation into the impact of incorporating the chiral ligand R-MBAPbI$_3$ into perovskite solar cells, with a particular focus on its influence on the Voc. By systematically varying the concentration of the chiral additive, we identified an optimal composition that enabled the device to reach a Voc of 1.17 V. Structural analysis via XRD confirmed that the integration of the chiral ligand introduced microstrain into the perovskite lattice, which played a crucial role in modifying the energy band structure. Such band structure modulation resulted in more favorable energy level alignment between the perovskite absorber and adjacent charge transport layers, enhancing charge carrier extraction while reducing recombination losses. EIS further supported this improvement, showing a marked decrease in non-radiative voltage loss from 354 mV in control devices to 304 mV in those containing *R*-MBAPbI$_3$. These results highlight the potential of chiral molecular engineering as an effective strategy for improving perovskite film uniformity and boosting device efficiency. Moreover, this approach

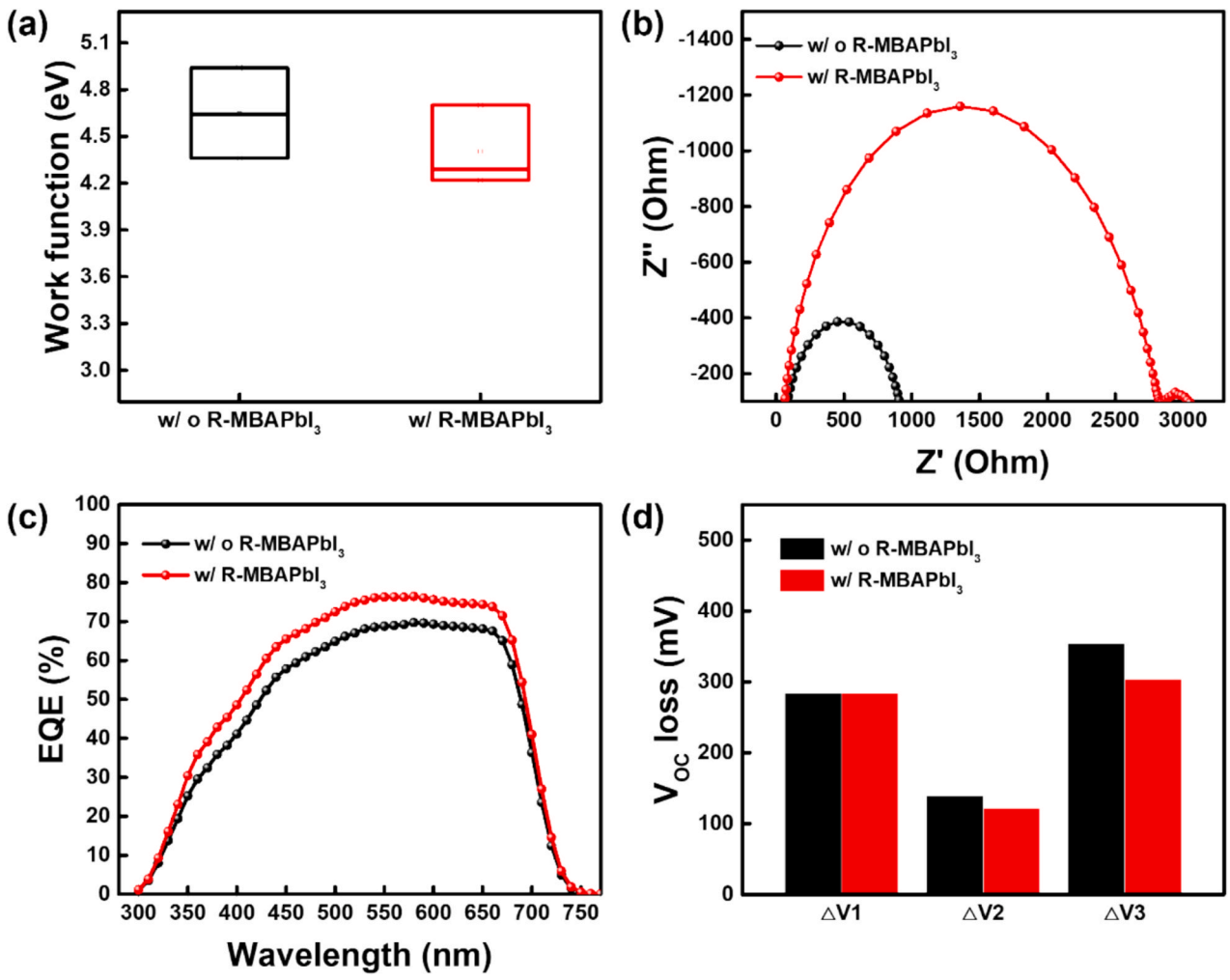

Fig. 5. Perovskite film with and without *R*-MBAPbI$_3$ additive. (a) Work function (b) Nyquist plots from Electrochemical impedance spectroscopy (EIS). (c) External quantum efficiency (EQE) and (d) V_{OC} loss.

Table 2
The V_{OC} loss of devices without and with *R*-MBAPbI$_3$.

R-MBAPbI$_3$	V_{OC}^{SC}(V)	V_{OC}(V)	ΔV_1(mV)	ΔV_2(mV)	ΔV_3(mV)
w/ o	1.48	1.11	284	139	354
w/		1.16	284	122	304

offers a promising and scalable pathway for narrowing the V_{OC} deficit, thus advancing perovskite photovoltaics toward their theoretical performance ceiling.

CRediT authorship contribution statement

Yu-Hung Hsiao: Writing – original draft, Validation, Methodology, Investigation, Formal analysis, Data curation. **Lan-Sheng Yang:** Writing – original draft, Investigation, Formal analysis. **Shih-Han Huang:** Writing – original draft, Validation, Formal analysis, Data curation. **Hou-Chin Cha:** Writing – review & editing, Funding acquisition, Formal analysis, Data curation. **Wen-Ting Li:** Formal analysis. **Sheng-Long Jeng:** Writing – review & editing. **Yu-Chiang Chao:** Writing – review & editing, Supervision, Resources, Funding acquisition. **Yu-Ching Huang:** Writing – review & editing, Supervision, Resources, Project administration, Funding acquisition, Conceptualization.

Declaration of Competing Interest

The authors declare that they have no known competing financial interests or personal relationships that could have appeared to influence the work reported in this paper.

Acknowledgements

This research was supported in full by the National Science and Technology Council of Taiwan with Grant Nos. NSTC 112-2622-E-131-011, NSTC 112-2628-E-131-001-MY4, NSTC 112-2628-M-003-002-MY3, NSTC 114-2927-I-003-501, NSTC 114-2222-E-131-002.

Appendix A. Supplementary data

Supplementary data to this article can be found online at https://doi.org/10.1016/j.solener.2025.114276.

Data availability

Data will be made available on request.

References

[1] H.J. Snaith, Perovskites: the emergence of a new era for low-cost, high-efficiency solar cells, J. Phys. Chem. Lett. 4 (2013) 3623–3630.

[2] A. Miyata, A. Mitioglu, P. Plochocka, O. Portugall, J.-T.-W. Wang, S.D. Stranks, H. J. Snaith, R.J. Nicholas, Direct measurement of the exciton binding energy and effective masses for charge carriers in organic–inorganic tri-halide perovskites, Nat. Phys. 11 (2015) 582–587.
[3] Z. Liang, Y. Zhang, H. Xu, W. Chen, B. Liu, J. Zhang, H. Zhang, Z. Wang, D.-H. Kang, J. Zeng, Homogenizing out-of-plane cation composition in perovskite solar cells, Nature 624 (2023) 557.
[4] D. Zhou, T. Zhou, Y. Tian, X. Zhu, Y. Tu, Perovskite-based solar cells: materials, methods, and future perspectives, J. Nanomater. 2018 (2018) 1–15.
[5] J.-P. Correa-Baena, M. Saliba, T. Buonassisi, M. Grätzel, A. Abate, W. Tress, A. Hagfeldt, Promises and challenges of perovskite solar cells, Science 358 (2017) 739–744.
[6] R. Xu, F. Pan, J. Chen, J. Li, Y. Yang, Y. Sun, X. Zhu, P. Li, X. Cao, J. Xi, Optimizing the buried interface in flexible perovskite solar cells to achieve over 24% efficiency and long-term stability, Adv. Mater. 36 (2024) 2308039.
[7] K.W. Kim, Y.-H. Seo, M.H. Ann, W. Lee, J. Nam, J. Chung, G. Seo, S. Nam, B.S. Ma, T.-S. Kim, Overcoming stability limitations of efficient, flexible perovskite solar modules, Joule 8 (2024) 13801393.
[8] H.S. Jung, G.S. Han, N.-G. Park, M.J. Ko, Flexible perovskite solar cells, Joule 3 (2019) 1850–1880.
[9] A. Rajagopal, Z. Yang, S.B. Jo, I.L. Braly, P.W. Liang, H.W. Hillhouse, A.K.Y. Jen, Highly efficient perovskite–perovskite tandem solar cells reaching 80% of the theoretical limit in photovoltage, Adv. Mater. 29 (2017) 1702140.
[10] D. Forgács, L. Gil-Escrig, D. Pérez-Del-Rey, C. Momblona, J. Werner, B. Niesen, C. Ballif, M. Sessolo, H.J. Bolink, Efficient monolithic perovskite/perovskite tandem solar cells, Adv. Energy Mater. 7 (2017) 1602121.
[11] J. Carrillo, A. Guerrero, S. Rahimnejad, O. Almora, I. Zarazua, E. Mas-Marza, J. Bisquert, G. Garcia-Belmonte, Ionic reactivity at contacts and aging of methylammonium lead triiodide perovskite solar cells, Adv. Energy Mater. 6 (2016) 1502246.
[12] H. Zhang, N.-G. Park, Progress and issues in p-i-n type perovskite solar cells, DeCarbon 3 (2024) 100025.
[13] Q. Wali, F.J. Iftikhar, M.E. Khan, A. Balilonda, M. Aamir, W. Fan, S. Yang, High efficiency (> 20%) and stable inverted perovskite solar cells: current progress and future challenges, J. Mater. Chem. C 10 (2022) 12908–12928.
[14] C.M. Wolff, P. Caprioglio, M. Stolterfoht, D. Neher, Nonradiative recombination in perovskite solar cells: the role of interfaces, Adv. Mater. 31 (2019) 1902762.
[15] W. Tress, M. Yavari, K. Domanski, P. Yadav, B. Niesen, J.P.C. Baena, A. Hagfeldt, M. Graetzel, Interpretation and evolution of open-circuit voltage, recombination, ideality factor and subgap defect states during reversible light-soaking and irreversible degradation of perovskite solar cells, Energy Environ. Sci. 11 (2018) 151–165.
[16] A. Buin, P. Pietsch, J. Xu, O. Voznyy, A.H. Ip, R. Comin, E.H. Sargent, Materials processing routes to trap-free halide perovskites, Nano Lett. 14 (2014) 6281–6286.
[17] L.-B. Huang, P.-Y. Su, J.-M. Liu, J.-F. Huang, Y.-F. Chen, S. Qin, J. Guo, Y.-W. Xu, C.-Y. Su, Interface engineering of perovskite solar cells with multifunctional polymer interlayer toward improved performance and stability, J. Power Sources 378 (2018) 483–490.
[18] H. Dong, J. Xi, L. Zuo, J. Li, Y. Yang, D. Wang, Y. Yu, L. Ma, C. Ran, W. Gao, Conjugated molecules "Bridge": functional ligand toward highly efficient and long-term stable perovskite solar cell, Adv. Funct. Mater. 29 (2019) 1808119.
[19] F. Ansari, E. Shirzadi, M. Salavati-Niasari, T. LaGrange, K. Nonomura, J.-H. Yum, K. Sivula, S.M. Zakeeruddin, M.K. Nazeeruddin, M. Grätzel, Passivation mechanism exploiting surface dipoles affords high-performance perovskite solar cells, J. Am. Chem. Soc. 142 (2020) 11428–11433.
[20] G. Zhang, Y. Zheng, Y. Shi, X. Ma, M. Sun, T. Li, B. Yang, Y. Shao, Improving the performance of perovskite solar cells with insulating additive-modified hole transport layers, ACS Appl. Mater. Interface 14 (2022) 11500–11508.
[21] H. Wang, Z. Zhang, X. Wang, L. Duan, J. Luo, Phenyltrimethylammonium chloride additive for highly efficient and stable $FAPbI_3$ perovskite solar cells, Nano Energy 123 (2024) 109423.
[22] D. Liu, H. Zheng, Y. Wang, L. Ji, H. Chen, W. Yang, L. Chen, Z. Chen, S. Li, Vacancies substitution induced interfacial dipole formation and defect passivation for highly stable perovskite solar cells, Chem. Eng. J. 396 (2020) 125010.
[23] T. Yang, W. Zhao, X. Liu, S. Liu, Tailoring the interfacial termination via dipole interlayer for high-efficiency perovskite solar cells, Adv. Energy Mater. 13 (2023) 2204192.
[24] G. Wu, R. Liang, M. Ge, G. Sun, Y. Zhang, G. Xing, Surface passivation using 2D perovskites toward efficient and stable perovskite solar cells, Adv. Mater. 34 (2022) e2105635.
[25] H.B. Lee, N. Kumar, V. Devaraj, B. Tyagi, S. He, R. Sahani, K.-J. Ko, J.-W. Oh, J.-W. Kang, Trifluoromethyl-group bearing, hydrophobic bulky cations as defect passivators for highly efficient, stable perovskite solar cells, Sol. RRL 5 (2021) 2100712.
[26] A.H. Proppe, A. Johnston, S. Teale, A. Mahata, R. Quintero-Bermudez, E.H. Jung, L. Grater, T. Cui, T. Filleter, C.-Y. Kim, Multication perovskite 2D/3D interfaces form via progressive dimensional reduction, Nat. Commun. 12 (2021) 3472.
[27] F. Wang, W. Geng, Y. Zhou, H.-H. Fang, C.-J. Tong, M.A. Loi, L.-M. Liu, N. Zhao, Phenylalkylamine passivation of organolead halide perovskites enabling high-efficiency and air-stable photovoltaic cells, Adv. Mater. 28 (2016) 9986–9992.
[28] C.T. Lin, J. Lee, J. Kim, T.J. Macdonald, J. Ngiam, B. Xu, M. Daboczi, W. Xu, S. Pont, B. Park, Origin of open-circuit voltage enhancements in planar perovskite solar cells induced by addition of bulky organic cations, Adv. Funct. Mater. 30 (2020) 1906763.
[29] R.P. Sabatini, C. Liao, S. Bernardi, W. Mao, M.S. Rahme, A. Widmer-Cooper, U. Bach, S. Huang, A.W. Ho-Baillie, G. Lakhwani, Solution-processed faraday rotators using single crystal lead halide perovskites, Adv. Sci. 7 (2020) 1902950.
[30] W.-J. Wei, X.-X. Jiang, L.-Y. Dong, W.-W. Liu, X.-B. Han, Y. Qin, K. Li, W. Li, Z.-S. Lin, X.-H. Bu, Regulating second-harmonic generation by van der Waals interactions in two-dimensional lead halide perovskite nanosheets, J. Am. Chem. Soc. 141 (2019) 9134–9139.
[31] H.-Y. Zhang, X.-J. Song, H. Cheng, Y.-L. Zeng, Y. Zhang, P.-F. Li, W.-Q. Liao, R.-G. Xiong, A three-dimensional lead halide perovskite-related ferroelectric, J. Am. Chem. Soc. 142 (2020) 4604–4608.
[32] M. Schulz, F. Balzer, D. Scheunemann, O. Arteaga, A. Lützen, S.C. Meskers, M. Schiek, Chiral excitonic organic photodiodes for direct detection of circular polarized light, Adv. Funct. Mater. 29 (2019) 1900684.
[33] C. Chen, L. Gao, W. Gao, C. Ge, X. Du, Z. Li, Y. Yang, G. Niu, J. Tang, Circularly polarized light detection using chiral hybrid perovskite, Nat. Commun. 10 (2019) 1927.
[34] Z.G. Wu, H.B. Han, Z.P. Yan, X.F. Luo, Y. Wang, Y.X. Zheng, J.L. Zuo, Y. Pan, Chiral octahydro-binaphthol compound-based thermally activated delayed fluorescence materials for circularly polarized electroluminescence with superior EQE of 32.6% and extremely low efficiency roll-off, Adv. Mater. 31 (2019) 1900524.
[35] H. Lee, M.J. Huttunen, K.-J. Hsu, M. Partanen, G.-Y. Zhuo, M. Kauranen, S.-W. Chu, Chiral imaging of collagen by second-harmonic generation circular dichroism, Biomed, Opt. Express 4 (2013) 909–916.
[36] S.K. Jung, J.H. Heo, B.M. Oh, J.B. Lee, S.H. Park, W. Yoon, Y. Song, H. Yun, J. H. Kim, S.H. Im, Chiral stereoisomer engineering of electron transporting materials for efficient and stable perovskite solar cells, Adv. Funct. Mater. 30 (2020) 1905951.
[37] Q. Zhou, B. Liu, Y. Chen, D. Ma, X. Han, D. He, Z. Zhang, H. Yang, P. Zhao, J. Hou, Managing photons and carriers by multisite chiral molecules achieving high-performance perovskite solar cells fabricated in ambient air, Nano Energy 124 (2024) 109512.
[38] X. Zhao, Z. Zhang, Y. Zhu, F. Meng, M. Li, C. Wang, W. Gao, Y. Feng, R. Li, D. He, Rationally tailoring chiral molecules to minimize interfacial energy loss enables efficient and stable perovskite solar cells using vacuum flash technology, Nano Lett. 23 (2023) 11184–11192.
[39] W. Gao, H. Dong, N. Sun, L. Chao, W. Hui, Q. Wei, H. Li, Y. Xia, X. Gao, G. Xing, Chiral cation promoted interfacial charge extraction for efficient tin-based perovskite solar cells, J. Energy Chem. 68 (2022) 789–796.
[40] Y. Huang, H. Luo, B. Zhang, K. Su, W. Chen, G. Sui, L. Liang, B. Zhang, J. Song, P. Gao, 2D or not 2D? Selectively formed low-dimensional perovskitoids based on chiral organic cation to passivate perovskite solar cells, Appl. Mater. Today 28 (2022) 101550.
[41] Y.-H. Wu, Y. Ding, X.-Y. Liu, X.-H. Ding, X.-P. Liu, X. Pan, S.-Y. Dai, Ambient stable $FAPbI_3$-based perovskite solar cells with a 2D-$EDAPbI_4$ thin capping layer, Sci. China Mater. 63 (2020) 47–54.
[42] C. Zhu, X. Niu, Y. Fu, N. Li, C. Hu, Y. Chen, X. He, G. Na, P. Liu, H. Zai, Strain engineering in perovskite solar cells and its impacts on carrier dynamics, Nat. Commun. 10 (2019) 815.
[43] T. Wang, L. Bi, L. Yang, Z. Zeng, X. Ji, Z. Hu, S.-W. Tsang, H.-L. Yip, Q. Fu, A.-K.-Y. Jen, Dimensional regulation from 1D/3D to 2D/3D of perovskite interfaces for stable inverted perovskite solar cells, J. Am. Chem. Soc. 146 (2024) 7555–7564.
[44] H. Cheng, C. Liu, J. Zhuang, J. Cao, T. Wang, W.Y. Wong, F. Yan, KBF_4 additive for alleviating microstrain, improving crystallinity, and passivating defects in inverted perovskite solar cells, Adv. Funct. Mater. 32 (2022) 2204880.
[45] C. Li, W. Liu, S. Da, L. Kong, F. Ran, Micro-strain regulation strategy to stabilize perovskite lattice based on the categories and impact of strain on perovskite solar cells, J. Energy Chem. 100 (2024) 578–604.
[46] W. Shockley, H. Queisser, Detailed balance limit of efficiency of p-n junction solar cells, J. Appl. Phys. 32 (1961) 510–519.
[47] J. Wang, J. Zhang, Y. Zhou, H. Liu, Q. Xue, X. Li, C.C. Chueh, H.L. Yip, Z. Zhu, A.K. Y. Jen, Highly efficient all-inorganic perovskite solar cells with suppressed non-radiative recombination by a Lewis base, Nat. Commun. 11 (2020) 177.